

RESEARCH PAPER

Observation of Small-amplitude Electromagnetic Cyclotron Waves in the Solar Wind

To cite this article: Hai-Feng Yang *et al* 2023 *Res. Astron. Astrophys.* **23** 045009


View the [article online](#) for updates and enhancements.

You may also like

- [Modeling very high electron heating by radio frequency waves on EAST](#)
Yueheng Huang, Nong Xiang, Jiale Chen et al.
- [Time-dependent Occurrence Rate of Electromagnetic Cyclotron Waves in the Solar Wind: Evidence for the Effect of Alpha Particles?](#)
G. Q. Zhao, H. Q. Feng, D. J. Wu et al.
- [The effects of kinetic instabilities on the electron cyclotron emission from runaway electrons](#)
Chang Liu, Lei Shi, Eero Hirvijoki et al.



Observation of Small-amplitude Electromagnetic Cyclotron Waves in the Solar Wind

Hai-Feng Yang^{1,2}, Guo-Qing Zhao^{1,2} , Heng-Qiang Feng^{1,2}, Gilbert Pi³, Qiang Liu^{1,2}, Liang Xiang^{1,2}, Qiu-Huan Li^{1,2}, and Dan-Yang Ren¹

¹ Institute of Space Physics, Luoyang Normal University, Luoyang 471934, China; zgqisp@163.com

² Henan Key Laboratory of Electromagnetic Transformation and Detection, Luoyang 471934, China

³ Faculty of Mathematics and Physics, Charles University, Prague 121 16, Czech Republic

Received 2022 December 28; revised 2023 February 13; accepted 2023 February 15; published 2023 March 24

Abstract

Our previous studies on low-frequency electromagnetic cyclotron waves (ECWs) with amplitudes larger than 0.1 nT in the solar wind revealed that the left-handed (LH) polarized ECWs are the dominant waves, and these waves preferentially occur in plasma conditions of high proton speed (V_p), high proton temperature (T_p), low proton density (N_p). In the present study, using magnetic field and plasma data from the Wind mission between 2005 and 2015, we perform a survey of small-amplitude ECWs with amplitudes smaller than 0.1 nT. It is revealed for the first time that the small-amplitude right-handed (RH) polarized ECWs tend to frequently occur in plasmas characterized by low V_p , low T_p , low N_p , although the small-amplitude LH ECWs still preferentially occur in plasma conditions similar to the LH ECWs with amplitudes larger than 0.1 nT. Further investigation shows that the occurrences of small-amplitude RH ECWs and long-lasting radial interplanetary magnetic field (IrIMF) share the similar preferential plasma conditions of low T_p and low N_p . During IrIMF events, in particular, the occurrence rates of RH and LH ECWs are comparable, with the occurrence rate of small-amplitude RH ECWs slightly larger than that of small-amplitude LH ECWs. The generation mechanism of the small-amplitude ECWs is discussed.

Key words: (Sun:) solar wind – magnetic fields – waves

1. Introduction

The nonthermal ions in the solar wind may serve as free-energy sources to excite kinetic waves (Hollweg 1975; Schwartz 1980; Tu & Marsch 1995; Marsch et al. 2004; Marsch 2006; Cranmer 2014; He et al. 2015; Hellinger & Trávníček 2016; Klein et al. 2018; Wilson et al. 2018). Among these waves, low-frequency electromagnetic cyclotron waves (ECWs) near the proton cyclotron frequency are of interest in recent years. According to observations (Jian et al. 2009, 2010, 2014; Boardsen et al. 2015; Gary et al. 2016; Zhao et al. 2017b, 2018, 2019a, 2019b; Pi et al. 2022), ECWs are characterized by a typical frequency of 0.1–0.5 Hz around 1 au and are transverse waves propagating mainly in the direction parallel or antiparallel to ambient magnetic field (\mathbf{B}). The waves can be left-handed (LH) or right-handed (RH) polarized with respect to \mathbf{B} in the spacecraft frame. Most of the observations show that the waves are usually dominated by LH polarization, and the occurrence rate of LH ECWs is more than twice of the occurrence rate of RH ECWs (Zhao et al. 2017b; Yang et al. 2022). LH ECWs tend to occur in the regions of high proton speed (V_p), high proton temperature (T_p), low proton density (N_p) and alpha-proton differential flow (V_d) pointing anti-sunward, where $V_d = V_\alpha - V_p$ and V_α and V_p are velocities of alpha particles and protons, respectively.

To clarify the generation mechanisms of ECWs, plasma instabilities driven by temperature anisotropies and/or differential flows between ion populations are proposed (Gary et al. 1993; Li & Habbal 2000; Lu et al. 2006; Verscharen et al. 2013; Omidi et al. 2014). It is believed that ion cyclotron waves (LH ECWs in the plasma frame) are produced by the proton cyclotron instability excited by temperature anisotropies with perpendicular temperature higher than parallel temperature, and magnetosonic waves (RH ECWs in the plasma frame) are produced by the firehose instability excited by the converse temperature anisotropy (Jian et al. 2010; Podesta & Gary 2011a, 2011b; Xiang et al. 2020, 2021). The ion cyclotron waves or magnetosonic waves can also be excited at the presence of large beam-core differential flows (Abraham-Shrauner et al. 1979; Gary et al. 1993; Daughton & Gary 1998; Daughton et al. 1999; Goldstein et al. 2000; Xiang et al. 2018a, 2018b), or large alpha-proton differential flow (Wicks et al. 2016; Zhao et al. 2017b, 2019a, 2019b, 2020; Yang et al. 2022). For combined effects of temperature anisotropies and differential flows, previous research tends to suggest that the main driver of instabilities is temperature anisotropies, but differential flows provide additional free energy and amplify the wave growth in the solar wind (Jian et al. 2016; Wicks et al. 2016; Zhao et al. 2017b, 2019a, 2019b).

Despite recent observational and theoretical works, some questions about the occurrence of ECWs remain open. First, previous research mostly focused on ECWs with amplitudes larger than a certain threshold (such as 0.1 nT in Zhao et al. 2017a, 2017b, 2018, 2019a, 2019b; Yang et al. 2022), and a detailed study on small-amplitude ECWs is lacking. Second, the preferential plasma conditions for the occurrence of RH ECWs are ambiguous, at least not as clear as those for LH ECWs. In this paper, we pay much attention to the occurrence of small-amplitude ECWs, which may be helpful for a deeper understanding of the occurrence of ECWs.

The solar wind carrying a frozen-in magnetic field streams outward from the Sun and permeates the interplanetary space, creating the interplanetary magnetic field (IMF). The IMF usually has a spiral structure and the direction is expected to be around 45° away from the Sun–Earth line near the Earth according to Parker’s model (Parker 1958). However, some exceptions have been found, such as long-lasting radial IMF (lrIMF) events observed by Ulysses (Jones et al. 1998; Gosling & Skoug 2002; Murphy et al. 2002), ISEE-3 (Neugebauer et al. 1997), OMNI (Pi et al. 2014), ACE (Orlove et al. 2013) and Wind (Pi et al. 2022). These observations show that the solar wind during lrIMF events is characterized by low N_p , low T_p and decreasing V_p (Riley & Gosling 2007; Pi et al. 2014). The bulk speed difference between the beginning and ending of lrIMF is usually considered to be the main factor creating lrIMF (Gosling & Skoug 2002; Schwadron 2002; Riley & Gosling 2007; Orlove et al. 2013). It is found that the lrIMF events play an important role in activities in Sun–Earth space, such as space weather, the location and shape of the magnetopause, bow shock effects, and formation of the dayside magnetopause and its boundary layers (Pi & Němeček 2018; Pi et al. 2022). However, minimal attention has been given to the effect of the lrIMF events on the occurrence of ECWs (Pi et al. 2022). In this paper, we also investigate the occurrence of ECWs during the lrIMF events in detail, which may reveal the characteristics of the occurrence of ECWs during the specific IMF.

2. Data and Analysis Methods

In this study, observations were made between 2005 and 2015 using data from the Wind mission, which had a halo orbit around the L1 Lagrange point during this time. Specifically, the magnetic field data are from the Magnetic Field Investigation (MFI) instrument on board the Wind mission sampled at a cadence of 0.092 s (Lepping et al. 1995). The plasma data are from the Solar Wind Experiment (SWE) instrument (Ogilvie et al. 1995) and are produced via a nonlinear-least-squares bi-Maxwellian fitting of the ion spectrum measured by the Faraday cup with a cadence of 92 s (Kasper et al. 2006). In addition, we discarded all data with V_d/V_p less than 1% and with the angle between V_d and \mathbf{B} (or $-\mathbf{B}$) greater than 20° to exclude the observations of V_d with a large uncertainty (Kasper et al. 2006; Alterman et al. 2018).

An automatic wave detection procedure (Zhao et al. 2017b, 2018) is employed to conduct a study of ECWs based on the magnetic field data. We briefly describe the main steps as follows. First, reduced magnetic helicity (Matthaeus & Goldstein 1982; Matthaeus et al. 1982; Gary & Winske 1992; He et al. 2011) and transverse power spectrum for a magnetic field interval are calculated. Second, the magnetic helicity spectrum and the transverse power spectrum are examined in the frequency range from 0.05 to 1 Hz. The presence of an ECW event is identified if the magnetic helicity has an absolute value greater than 0.7 in some frequency band with a minimum bandwidth of 0.05 Hz and the transverse wave power is three times larger than the background power in the same frequency band. Finally, unlike previous studies (Zhao et al. 2017a, 2017b, 2018, 2019a, 2019b; Yang et al. 2022), we took advantage of all ECWs including small-amplitude waves in this study.

Magnetic field data have also been used to identify lrIMF events. The criteria for lrIMF intervals are the same as that adopted by Pi et al. (Pi et al. 2014, 2022). The ratio of the B_x magnetic field component and its magnitude B should be larger than 0.9 for four or more hours, but a short break (less than 15 minutes) is allowed. Based on wind observations between 2005 and 2015, 319 lrIMF events were found, accounting for 2.55% of the total time. It should be noted that if the criteria (value of $|B_x|/B$ and the breaking time) are slightly changed, we will have different numbers and intervals of lrIMF events, but this does not change the main conclusions of this study.

3. Statistical Results

Using the plasma and magnetic field data from the Wind mission, we investigate the occurrence of ECWs at different kinds of wave amplitudes and IMFs. Observations of small-amplitude ECWs are presented in Section 3.1. An investigation of the occurrence of ECWs, with particular attention to small-amplitude RH ECWs, is presented in Section 3.2. The solar wind characteristics and the occurrence rates of ECWs during lrIMF events are given in Section 3.3. Note that the wave polarization is described in the spacecraft frame throughout the paper, except when we point out the plasma frame.

3.1. Observation of Small-amplitude ECWs

Unlike previous work, this study focuses on small-amplitude ECWs with amplitudes smaller than 0.1 nT. Figure 1 shows an example of the identification of small-amplitude ECWs. First, the raw magnetic fields in geocentric solar ecliptic (GSE) coordinates are changed into field-aligned coordinates (Gao et al. 2014; Zhao et al. 2017a), and the transverse components are given in Figure 1(a). Second, the raw magnetic fields in field-aligned coordinate are transformed from the time domain to the frequency domain by the fast Fourier transform, and the magnetic helicity spectrum and the transverse power spectrum

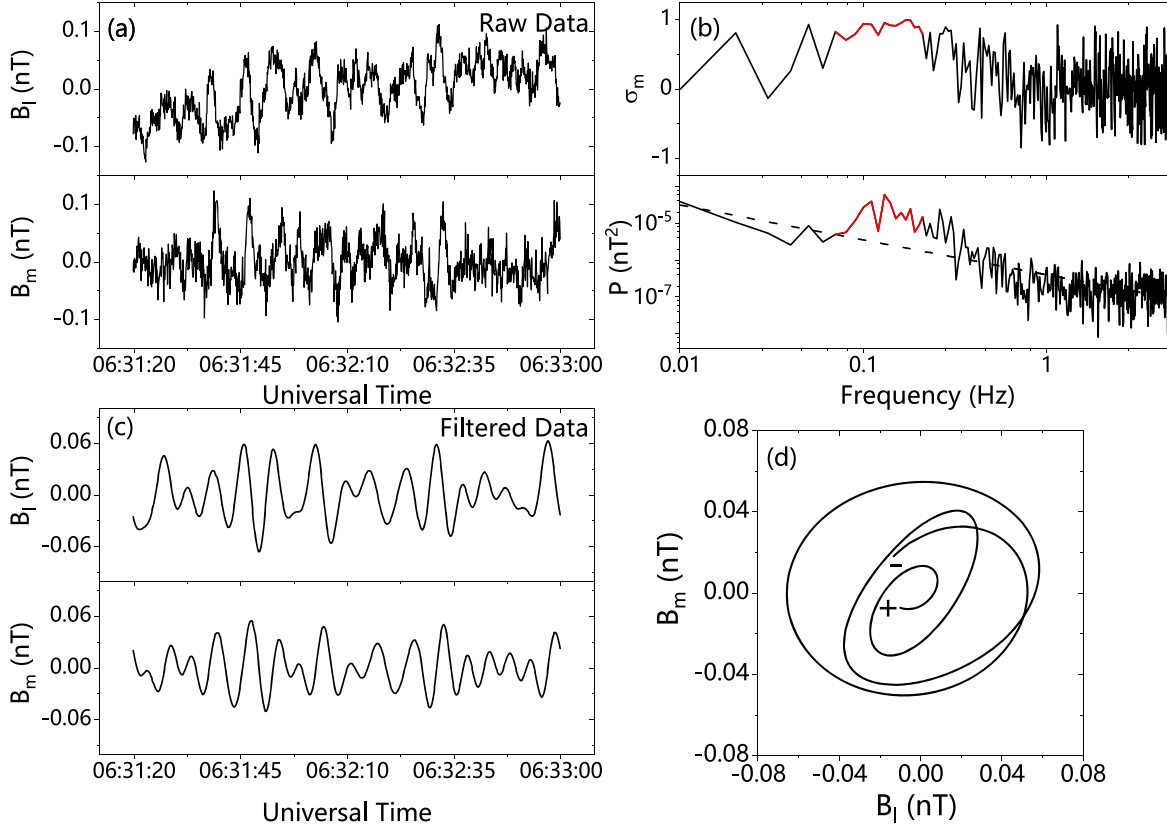


Figure 1. Illustration of the identification of small-amplitude ECWs. The transverse components of the raw magnetic field (a) and the filtered magnetic field (c) in the field-aligned coordinate system on 2006 November 9. (b) The magnetic helicity spectrum σ_m (upper panel) and the transverse power spectrum (lower panel). The red lines in (b) mark the frequency band with σ_m greater than 0.7 and the dashed line in the lower panel of (b) represents the power law fitting for the transverse power spectrum. (d) Hodogram of filtered transverse components with a time interval of 20 s. The plus and minus signs indicate the beginning and end of the time series, respectively.

are obtained in Figure 1(b). We highlight the frequency band with σ_m greater than 0.7 in red and plot the power law fitting for the transverse power spectrum with dashed line. The strong positive magnetic helicity and enhanced transverse power spectrum indicate the appearance of an RH ECW. Finally, the waveforms after bandpass filtering are displayed in Figures 1(c), and the wave amplitude is determined to be 0.06 nT. In addition, Figure 1(d) shows the hodogram of the filtered transverse components with a time interval of 20 s, where the plus and minus signs mark the beginning and the end of the time series, respectively. It reveals that the wave is RH polarized in the spacecraft frame, consistent with a positive value of the magnetic helicity shown in Figure 1(b).

Based on the wave identification procedure described above, we obtain the numbers of LH and RH ECWs and the percentage of RH ECW against wave amplitude in Figure 2. According to Figure 2(a), 51.5% of RH ECWs and 39.2% of LH ECWs have amplitudes smaller than 0.1 nT, which were discarded in the previous studies (Zhao et al. 2017a, 2017b, 2018, 2019a, 2019b; Yang et al. 2022).

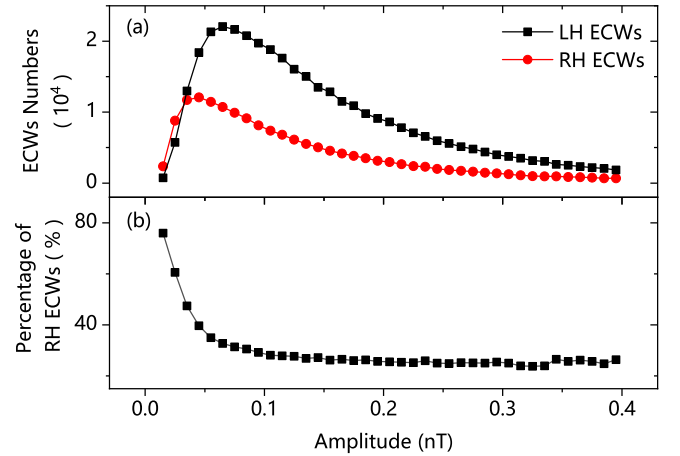


Figure 2. (a) The numbers of LH (black square line) and RH (red circle line) ECWs. (b) The percentage of RH ECWs against wave amplitude.

Figure 2(b) shows that the percentage of RH ECWs is nearly constant around 27% at amplitudes larger than 0.1 nT, which is consistent with previous observations that LH ECWs are the dominant waves (Zhao et al. 2017b; Yang et al. 2022).

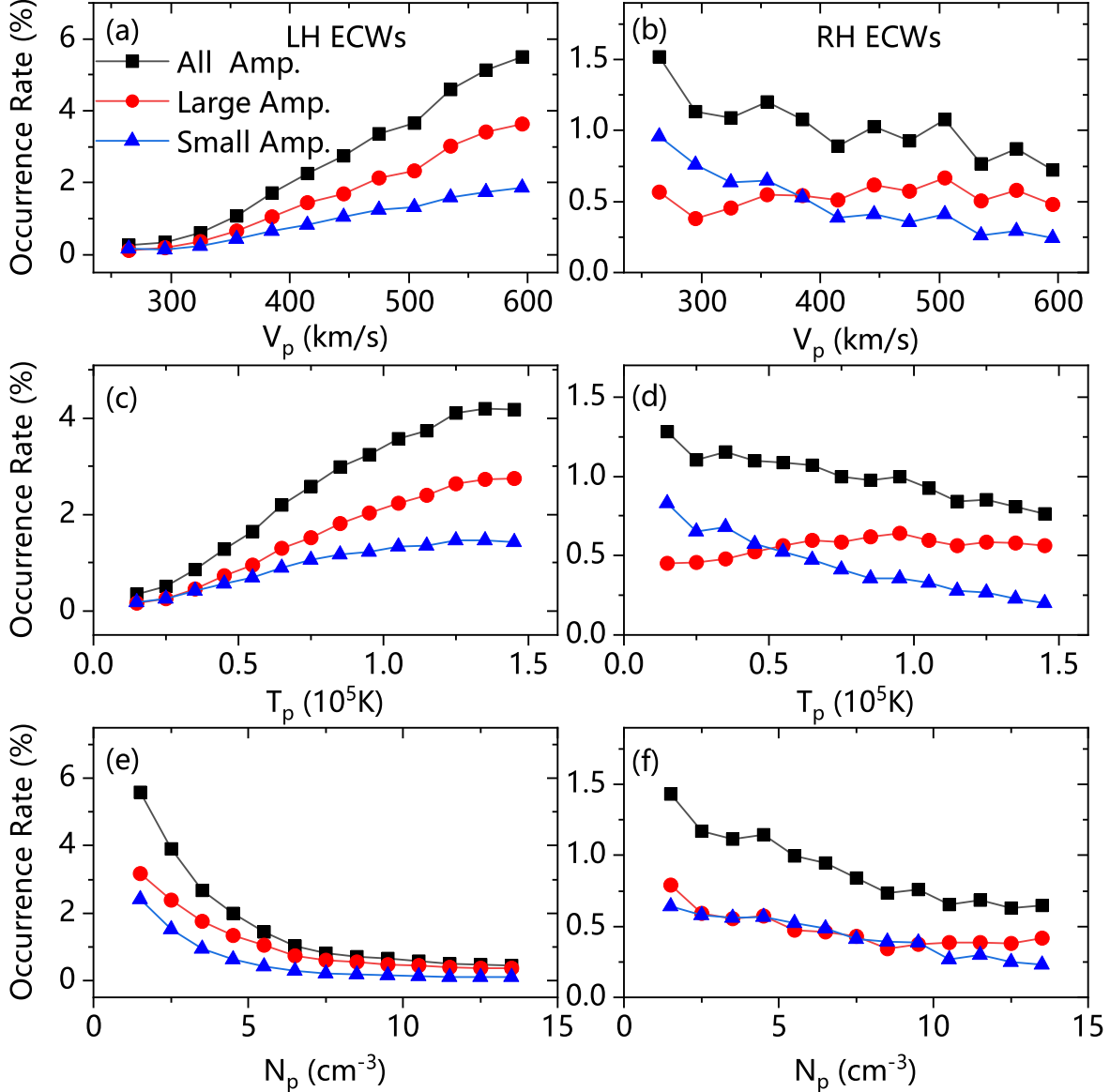


Figure 3. Occurrence rates of LH (left panel) and RH (right panel) ECWs with respect to V_p (a), (b), T_p (c), (d) and N_p (e), (f). The black square, red circle and blue triangle lines are for ECWs with all amplitudes, large amplitudes (>0.1 nT) and small amplitudes (<0.1 nT), respectively.

Furthermore, the percentage of RH ECWs increases rapidly as the amplitude decreases and RH ECWs become the dominant waves at amplitudes smaller than 0.04 nT.

3.2. Dependence of Occurrence of Small-amplitude ECWs on Plasma Parameters

In order to study the occurrence of ECWs including the small-amplitude waves, we present the occurrence rates of LH and RH ECWs with all amplitudes, large-amplitude (>0.1 nT) and small-amplitude (<0.1 nT) in Figure 3. The occurrence rate is defined as the ratio of the ECW number and the total sample

number in a certain parameter bin. The occurrence rates are calculated with respect to V_p , T_p and N_p . Examining LH ECWs in the left panels of Figure 3, the occurrence rates of large- and small-amplitude waves have almost the same trend of change, and the preferential plasma conditions for the occurrence of LH ECWs include high V_p , high T_p and low N_p , which is consistent with the conclusions of the previous papers (Zhao et al. 2017b; Yang et al. 2022). In particular, on inspection of the RH ECWs in the right panels of Figure 3, the occurrence rates of small-amplitude waves show clear dependence on the three plasma parameters, while the dependence is absent or negligible for

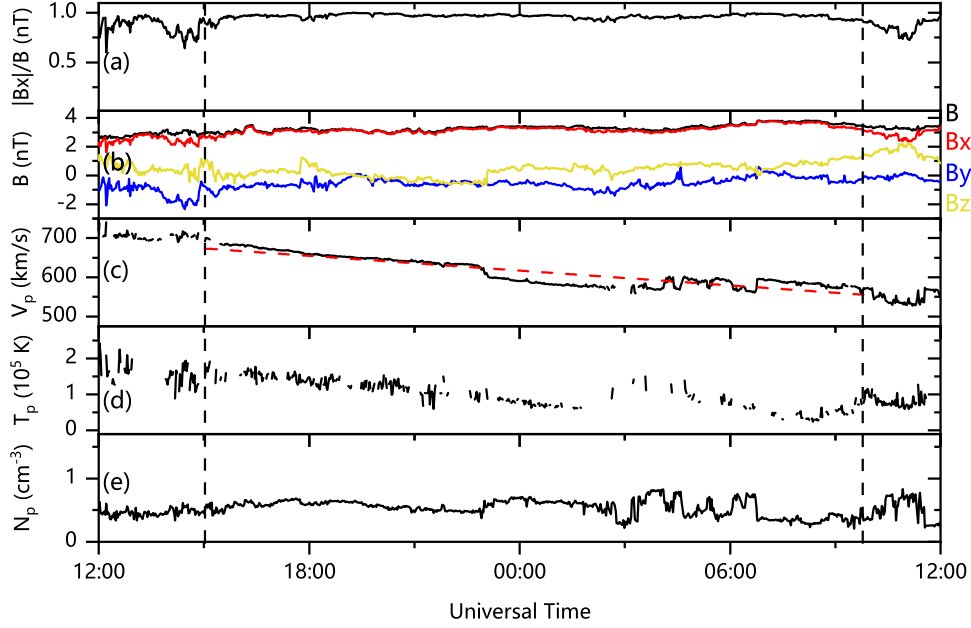


Figure 4. An example of a lrIMF event observed by Wind on 2013 May 28–29. From top to bottom: (a) $|B_x|/B$, (b) magnitude and three components of \mathbf{B} in GSE coordinates (red for B_x , blue for B_y , yellow for B_z), (c) V_p , (d) T_p , (e) N_p . The two vertical dashed lines denote the start and end times of the lrIMF event. The red dashed line in Figure 4(c) represents a linear fitting of V_p during the lrIMF event.

large-amplitude waves, which is in contrast to the case of LH ECWs. Specifically, we identify the preferential plasma conditions for the occurrence of small-amplitude RH ECWs including low V_p , low T_p and low N_p for the first time.

3.3. Occurrence of Small-amplitude ECWs during lrIMF Events

The study of wave activities during lrIMF events may be helpful for our understanding of the occurrence of small-amplitude ECWs. Figure 4 shows an example of a lrIMF event with a duration of up to 19 hr. The two vertical dashed lines indicate the start and end times of the lrIMF event. Figure 4(a) displays the value of $|B_x|/B$, and Figure 4(b) presents the magnitude and three components of \mathbf{B} in GSE coordinates. During the period between 15:03 on May 28 and 10:12 on May 29, the values of B and B_x are nearly equal with the ratio $|B_x|/B$ above 0.9, indicating the occurrence of a lrIMF event. Before or after the period, the values are highly variable. Figure 4(c) displays V_p and its linear fitting. The V_p is found to decrease from 680 to 560 km s^{-1} at a rate of $-6.3 \text{ km s}^{-1} \text{ h}^{-1}$ during the lrIMF event. Figures 4(d) and (e) show that the values of T_p and N_p change around their medians of $1.4 \times 10^5 \text{ K}$ and 0.57 cm^{-3} during this event.

To obtain the characteristics of the solar wind during lrIMF events, the variations of the yearly medians of solar wind parameters V_p , T_p , and N_p during all intervals, radial IMF (rIMF) events and lrIMF events are displayed in Figure 5. One may find that lrIMF events tend to occur in

regions of low T_p and low N_p . We also give the yearly medians of solar wind parameters during rIMF events without duration restriction to distinguish the effects of long-lasting and radial. It is shown that rIMF events tend to occur at low N_p , and that low T_p may be the key factor for the long-term persistence of the rIMF events. In addition, Figure 5(a) shows that the medians of V_p at the three conditions almost coincide, though it is usually believed that most of lrIMF events tend to occur at decreasing V_p as shown in Figure 4(c) and previous studies (Neugebauer et al. 1997; Pi et al. 2014).

The occurrences of small-amplitude RH ECWs and lrIMF events share the same preferential plasma conditions of low T_p and low N_p . Therefore, an increase in the occurrence rate of RH ECWs during lrIMF events may be expected when small-amplitude waves are included. Table 1 lists the occurrence rates of ECWs and the percentages of RH ECWs at different kinds of IMFs and amplitudes. Some conclusions about small-amplitude ECWs can be drawn from Table 1. During all intervals, the occurrence rate of LH ECWs is larger than that of RH ECWs. When the IMF is constrained to be radial (i.e., rIMF or lrIMF), the occurrence rates of both LH and RH ECWs increase. During rIMF events, the occurrence rates of both LH and RH ECWs more than quadruple, and thus the percentage of RH ECWs is almost unchanged. During lrIMF events, the increase of the occurrence rate of RH ECWs is significantly obvious than that of LH ECWs, resulting in a slightly larger occurrence rate of RH ECWs than that of LH ECWs (Pi et al. 2022). This

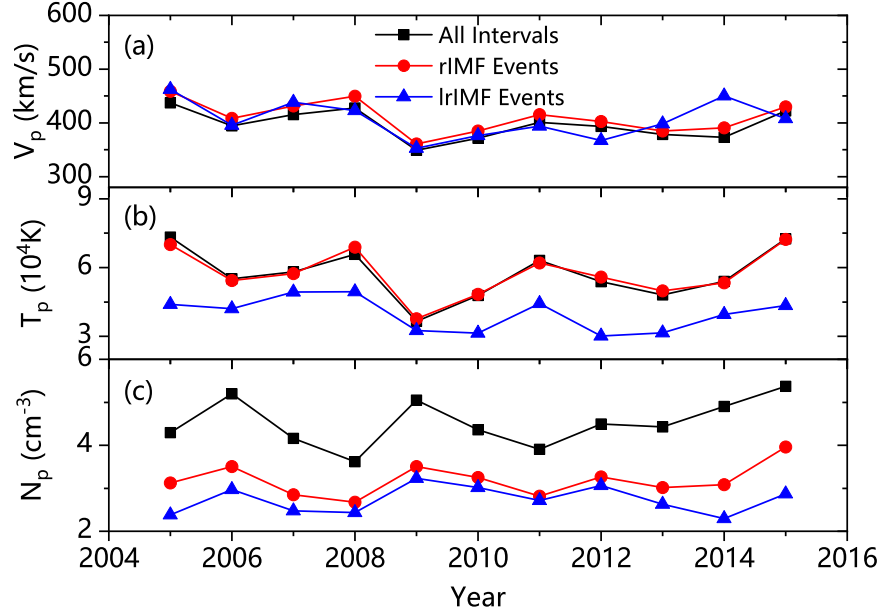


Figure 5. Yearly medians of V_p (a), T_p (b) and N_p (c) during all intervals (black square line), radial IMF (rIMF) events (red circle line) and lrIMF events (blue triangle line).

Table 1
Occurrence Rates and Percentages of ECWs at Different Kinds of IMFs and Amplitudes

IMFs Amplitudes	All Intervals			rIMF Events			lrIMF Events		
	All	Large	Small	All	Large	Small	All	Large	Small
Occurrence Rate of LH ECWs (%)	2.36	1.50	0.86	8.64	4.82	3.82	6.65	3.36	3.29
Occurrence Rate of RH ECWs (%)	1.05	0.54	0.51	3.86	1.74	2.12	6.86	2.83	4.03
Percentages of RH ECWs (%)	30.8	26.5	37.2	30.9	26.5	35.7	50.1	45.7	55.1

is different from previous observations that LH ECWs are the dominant waves (Zhao et al. 2017b; Yang et al. 2022). Furthermore, the percentage of RH ECWs with large amplitudes is smaller than that with small amplitudes for the three kinds of IMFs.

We also examine the dependence of the probability density distributions (PDDs) of the ambient plasma and the occurrence rates of ECWs on the V_d direction, as shown in Figure 6. The PDD is calculated as the ratio of the number of observations in each particular bin and the total number of observations. The angle between V_d and \mathbf{R} (the radial vector of the Sun) is defined as θ_{VdR} , and an angle θ_{VdR} less than 90° means that V_d is pointing anti-sunward while an angle θ_{VdR} greater than 90° denotes the sunward direction. Figure 6(a) displays the PDDs of the ambient plasma against θ_{VdR} during all intervals, rIMF events and lrIMF events, respectively. It is shown that the PDD has the maximums when θ_{VdR} is around 60° and 120° during all intervals. When the IMF is constrained to be radial (i.e., rIMF or lrIMF), the PDD has the maximums when θ_{VdR} is

around 15° and 165° where V_d is roughly parallel or anti-parallel to \mathbf{R} . In addition, the PPD with sunward V_d is significantly smaller than that with anti-sunward V_d during rIMF events, while the PPD with sunward V_d is only slightly smaller than that with anti-sunward V_d during lrIMF events. Figures 6(b)–(d) display the percentages of RH ECWs and the occurrence rates of ECWs with respect to θ_{VdR} . It is shown that RH (LH) ECWs are the dominant waves at sunward (anti-sunward) V_d . In addition, Figures 6(b)–(d) also show that the dependences of percentages and occurrence rates of RH ECWs on θ_{VdR} are more obvious for small-amplitude waves than for large-amplitude waves.

4. Discussion and Summary

The dependence of the occurrence of ECWs on θ_{VdR} revealed by Figures 6(b)–(d) may be explained by the linear Vlasov–Maxwell kinetic theory (Podesta & Gary 2011a), which indicates that LH (RH) ECWs in the plasma frame are preferentially generated by electromagnetic ion cyclotron

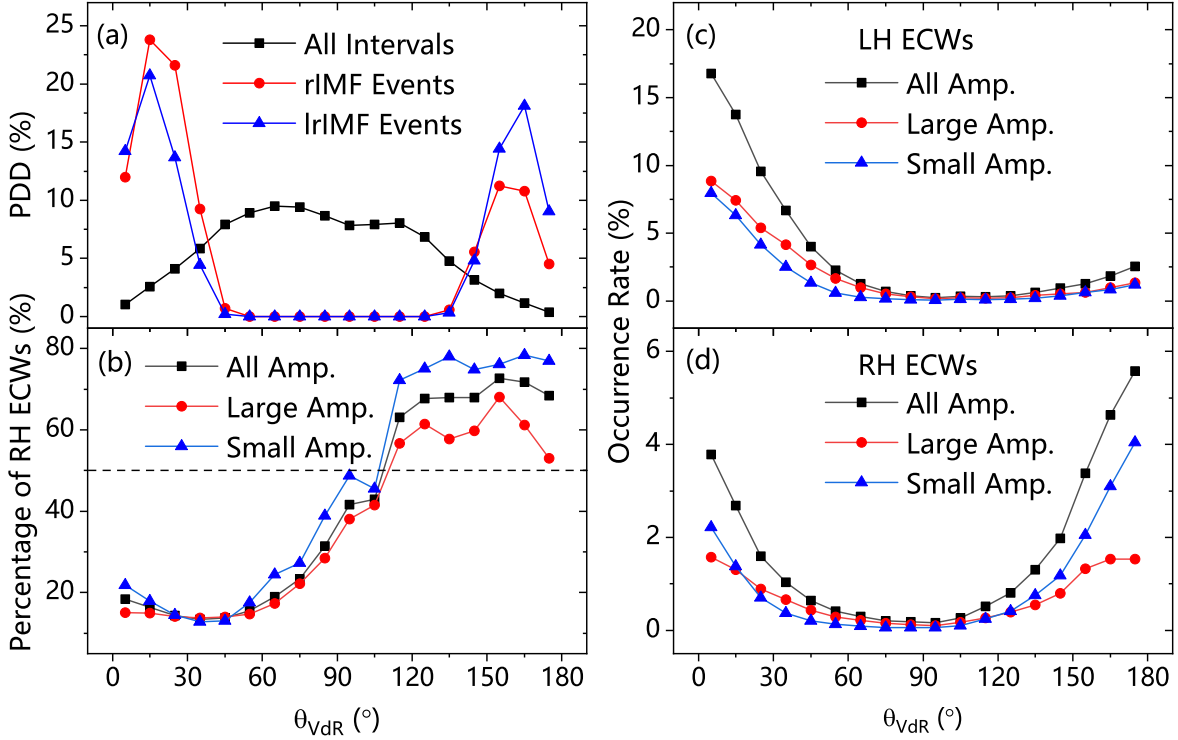


Figure 6. (a) Probability density distributions (PDDs) of the ambient plasma with respect to θ_{VdR} , where θ_{VdR} is the angle between V_d and R (the radial vector of the Sun). The black square, red circle and blue triangle lines are for all intervals, rIMF events and IrIMF events, respectively. Percentages of RH ECWs (b), and occurrence rates of LH (c) and RH (d) ECWs with respect to θ_{VdR} . The black square, red circle and blue triangle lines are for ECWs with all amplitudes, large amplitudes (>0.1 nT) and small amplitudes (<0.1 nT), respectively. The dashed line in Figure 6(b) indicates a value of 50%.

instability (parallel firehose instability) with a maximum growth rate occurring at $k \cdot V_d > 0$ ($k \cdot V_d < 0$), where k is the wavevector. This theory also means that LH ECWs in the spacecraft frame are the dominant waves when V_d is anti-sunward, while RH ECWs are the dominant waves when V_d is sunward, where the polarization reversal for ECWs with sunward k has been considered due to a large Doppler shift from the fast motion of the solar wind (Podesta & Gary 2011a; Yang et al. 2022). Then, we try to use the conclusions of Figure 6 to understand the changes in the occurrence rates of ECWs with all amplitudes in Table 1. When the IMF is constrained to be radial as shown in Figure 6(a), the increase in the PPD with V_d roughly parallel or anti-parallel to R may result in large occurrence rate of ECWs during rIMF or IrIMF events in Table 1. During rIMF events, the PDDs of the ambient plasma with anti-sunward V_d are significantly larger than those with sunward V_d , most likely resulting in a larger occurrence rate of LH ECWs than RH ECWs. During IrIMF events, the PDDs of the ambient plasma with the sunward and anti-sunward V_d are similar, which may be the reason for the similar occurrence rates of LH and RH ECWs as shown in Table 1.

Two findings about the occurrence of ECWs with small amplitudes are worth noting. First, the percentage of RH ECWs

increases as the amplitude decreases during all intervals as shown in Figure 2. Second, the occurrence rate of small-amplitude RH ECWs is slightly larger than that of small-amplitude LH ECWs during IrIMF events as shown in Table 1. These may be interpreted in the context of the temperature-anisotropy-driven instabilities with the effect of alpha particles. According to the theoretical study by Podesta & Gary (2011a), a small value of V_d/V_A and a weak temperature anisotropy correspond to a small growth rate for both the electromagnetic ion cyclotron instability and the parallel firehose instability, possibly resulting in waves with small amplitudes. Figure 7 displays the PDDs of $(\theta_{VdR}, T_{\perp}/T_{\parallel})$ and $(\theta_{VdR}, V_d/V_A)$ for all intervals and IrIMF events. A value of T_{\perp}/T_{\parallel} close to 1 implies weak temperature anisotropy. Figure 7 shows that the ambient plasma with sunward V_d , where RH ECWs dominate, has weaker temperature anisotropy and smaller value of V_d/V_A compared with that with anti-sunward V_d , where LH ECWs dominate. Then, RH ECWs may have smaller growth rate of instabilities and thus smaller amplitudes than LH ECWs, and the proportion of RH ECWs is larger when wave amplitude is smaller.

Note that in the above study we use the absolute amplitude of 0.1 nT as the criterion to distinguish small-amplitude from large-amplitude ECWs. We also carry out statistical analysis

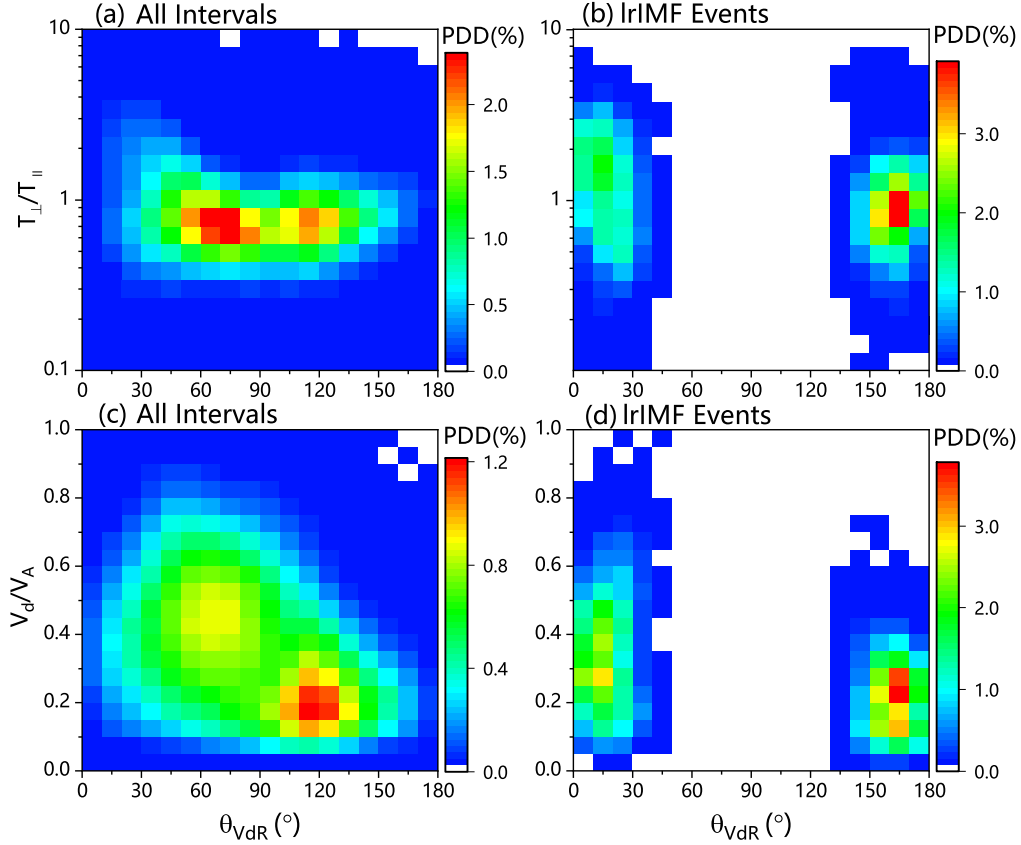


Figure 7. PDDs of $(\theta_{VdR}, T_{\perp}/T_{\parallel})$ (upper panels) and $(\theta_{VdR}, V_d/V_A)$ (lower panels) for ambient plasma. The left and right panels are for all intervals and IrIMF events, respectively.

adopting relative amplitude criterion of 0.02 to classify ECWs, where the relative amplitude is defined as the absolute amplitude normalized by the ambient magnetic field. The statistical results (not shown) qualitatively reproduce the trends of occurrence rate of ECWs using the absolute amplitude criterion (Figure 3). The occurrence rate and percentage of small-amplitude RH ECWs during IrIMF events are 3.21% and 54.2% respectively, indicating a slightly larger occurrence rate of small-amplitude RH ECWs than that of LH ECWs, which is also similar to the result using the absolute amplitude criterion (Table 1). Further studies on the PDDs of the relative and absolute amplitudes show that the relative amplitude is roughly proportional to the absolute amplitude (Figure 8) and there is no evident dependence of the absolute amplitude on the ambient magnetic field, which could result in the similar statistical results for the relative and absolute amplitude criteria.

In summary, we investigated the occurrences of ECWs with different amplitudes using the data from the Wind mission. It

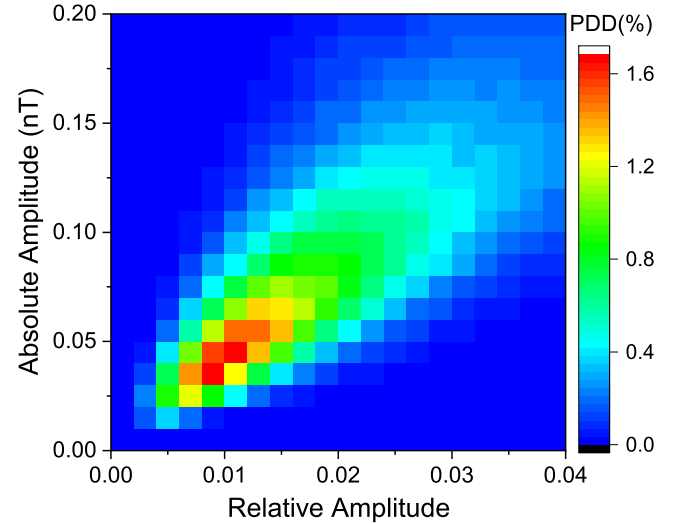


Figure 8. PDDs of (Relative Amplitude, Absolute Amplitude) for all the ECWs.

was found that small-amplitude LH ECWs preferentially occur in plasma conditions similar to large-amplitude cases. However, the preferential plasma conditions for the occurrence of small-amplitude RH ECWs are identified as low V_p , low T_p , low N_p , which are absent or negligible for large-amplitude RH ECWs. In addition, the occurrences of small-amplitude RH ECWs and IrIMF events share the similar preferential plasma conditions of low T_p and low N_p . When the IMF is constrained to IrIMF, the occurrence rates increase for both LH and RH ECWs, while the increase for RH ECWs is more obvious than that for LH ECWs, resulting in a slightly larger occurrence rate for RH ECWs than that for LH ECWs with small amplitudes. The generation mechanism of the small-amplitude ECWs could be the temperature-anisotropy-driven instabilities with the effect of alpha particles.

Acknowledgments

This research was supported by NSFC under grant Nos. 42174202, 41874204, 41974197, and 12103018. Research by G.-Q.Z. was supported partly by the Excellent Young Scientists Fund in Henan Province under grant No. 222300420061. The authors acknowledge the Wind mission for the data, which can be obtained via the Coordinated Data Analysis Web (http://cdaweb.gsfc.nasa.gov/cdaweb/istp_public/).

ORCID iDs

Guo-Qing Zhao  <https://orcid.org/0000-0002-1831-1451>

References

- Abraham-Shrauner, B., Asbridge, J. R., Bame, S. J., & Feldman, W. C. 1979, *JGR*, **84**, 553
- Alterman, B. L., Kasper, J. C., Stevens, M. L., & Koval, A. 2018, *ApJ*, **864**, 112
- Boardsen, S. A., Jian, L. K., Raines, J. L., et al. 2015, *JGRA*, **120**, 10207
- Cranmer, S. R. 2014, *ApJS*, **213**, 16
- Daughton, W., & Gary, S. P. 1998, *JGR*, **103**, 20613
- Daughton, W., Gary, S. P., & Winske, D. 1999, *JGR*, **104**, 4657
- Gao, X., Li, W., Thorne, R. M., et al. 2014, *JGRA*, **119**, 8992
- Gary, S. P., Anderson, B. J., Denton, R. E., et al. 1993, *Geophys. Res. Lett.*, **20**, 1767
- Gary, S. P., Jian, L. K., Broiles, T. W., et al. 2016, *JGRA*, **121**, 30
- Gary, S. P., & Winske, D. 1992, *JGR*, **97**, 3103
- Goldstein, B. E., Neugebauer, M., Zhang, L. D., & Gary, S. P. 2000, *Geophys. Res. Lett.*, **27**, 53
- Gosling, J. T., & Skoug, R. M. 2002, *JGRA*, **107**, 1327
- He, J., Marsch, E., Tu, C., Yao, S., & Tian, H. 2011, *ApJ*, **731**, 85
- He, J., Tu, C., Marsch, E., et al. 2015, *ApJL*, **813**, L30
- Hellinger, P., & Trávníček, P. M. 2016, *ApJ*, **832**, 32
- Hollweg, J. V. 1975, *RvGSP*, **13**, 263
- Jian, L. K., Moya, P. S., Viñas, A. F., & Stevens, M. 2016, SOLAR WIND 14: Proc. 14th Int. Solar Wind Conf., in AIP Conf. Proc., 1720, ed. L. Wang et al. (Melville, NY: AIP), 040007
- Jian, L. K., Russell, C. T., Luhmann, J. G., et al. 2009, *ApJL*, **701**, L105
- Jian, L. K., Russell, C. T., Luhmann, J. G., et al. 2010, *JGRA*, **115**, A12115
- Jian, L. K., Wei, H. Y., Russell, C. T., et al. 2014, *ApJ*, **786**, 123
- Jones, G. H., Balogh, A., & Forsyth, R. J. 1998, *Geophys. Res. Lett.*, **25**, 3109
- Kasper, J. C., Lazarus, A. J., Steinberg, J. T., Ogilvie, K. W., & Szabo, A. 2006, *JGRA*, **111**, A03105
- Klein, K. G., Alterman, B. L., Stevens, M. L., Vech, D., & Kasper, J. C. 2018, *PhRvL*, **120**, 205102
- Lepping, R. P., Acuña, M. H., Burlaga, L. F., et al. 1995, *SSRv*, **71**, 207
- Li, X., & Habbal, S. R. 2000, *JGR*, **105**, 7483
- Lu, Q. M., Wu, C. S., & Wang, S. 2006, *ApJ*, **638**, 1169
- Marsch, E. 2006, *LRSP*, **3**, 1
- Marsch, E., Ao, X.-Z., & Tu, C.-Y. 2004, *JGRA*, **109**, A04102
- Matthaeus, W. H., & Goldstein, M. L. 1982, *JGR*, **87**, 6011
- Matthaeus, W. H., Goldstein, M. L., & Smith, C. 1982, *PhRvL*, **48**, 1256
- Murphy, N., Smith, E. J., & Schwadron, N. A. 2002, *Geophys. Res. Lett.*, **29**, 2066
- Neugebauer, M., Goldstein, R., & Goldstein, B. E. 1997, *JGR*, **102**, 19743
- Ogilvie, K. W., Chornay, D. J., Fritzenreiter, R. J., et al. 1995, *SSRv*, **71**, 55
- Omididi, N., Isenberg, P., Russell, C. T., Jian, L. K., & Wei, H. Y. 2014, *JGRA*, **119**, 1442
- Orlove, S. T., Smith, C. W., Vasquez, B. J., et al. 2013, *ApJ*, **774**, 15
- Parker, E. N. 1958, *ApJ*, **128**, 664
- Pi, G., Němeček, Z., Áfránková, J., Grygorov, K., & Shue, J.-H. 2018, *JGRA*, **123**, 3533
- Pi, G., Pitňa, A., Zhao, G.-Q., et al. 2022, *Atmosphere*, **13**, 173
- Pi, G., Shue, J.-H., Chao, J.-K., et al. 2014, *JGRA*, **119**, 7005
- Podesta, J. J., & Gary, S. P. 2011a, *ApJ*, **742**, 41
- Podesta, J. J., & Gary, S. P. 2011b, *ApJ*, **734**, 15
- Riley, P., & Gosling, J. T. 2007, *JGRA*, **112**, A06115
- Schwadron, N. A. 2002, *Geophys. Res. Lett.*, **29**, 1663
- Schwartz, S. J. 1980, *RvGSP*, **18**, 313
- Tu, C.-Y., & Marsch, E. 1995, *SSRv*, **73**, 1
- Verscharen, D., Bourouaine, S., & Chandran, B. D. G. 2013, *ApJ*, **773**, 163
- Wicks, R. T., Alexander, R. L., Stevens, M., et al. 2016, *ApJ*, **819**, 6
- Wilson, L. B., III, Stevens, M. L., Kasper, J. C., et al. 2018, *ApJS*, **236**, 41
- Xiang, L., Lee, K. H., Wu, D. J., & Lee, L. C. 2020, *ApJ*, **899**, 61
- Xiang, L., Lee, K. H., Wu, D. J., Yu, H. W., & Lee, L. C. 2021, *ApJ*, **916**, 30
- Xiang, L., Wu, D. J., & Chen, L. 2018a, *ApJ*, **869**, 64
- Xiang, L., Wu, D. J., & Chen, L. 2018b, *ApJ*, **857**, 108
- Yang, H.-F., Zhao, G.-Q., Feng, H.-Q., et al. 2022, *RAA*, **22**, 065007
- Zhao, G. Q., Chu, Y. H., Lin, P. H., et al. 2017a, *JGRA*, **122**, 4879
- Zhao, G. Q., Feng, H. Q., Wu, D. J., Chu, Y. H., & Huang, J. 2017b, *ApJL*, **847**, L8
- Zhao, G. Q., Feng, H. Q., Wu, D. J., et al. 2018, *JGRA*, **123**, 1715
- Zhao, G. Q., Feng, H. Q., Wu, D. J., et al. 2020, *ApJL*, **889**, L14
- Zhao, G. Q., Feng, H. Q., Wu, D. J., Pi, G., & Huang, J. 2019a, *ApJ*, **871**, 175
- Zhao, G. Q., Li, H., Feng, H. Q., et al. 2019b, *ApJ*, **884**, 60